ADVANCED FUNCTIONAL MATERIALS
www.afm-journal.de

Direct Ink Writing of Polymer Composite Electrolytes with Enhanced Thermal Conductivities

*Meng Cheng, Ajaykrishna Ramasubramanian, Md Golam Rasul, Yizhou Jiang, Yifei Yuan, Tara Foroozan, Ramasubramonian Deivanayagam, Mahmoud Tamadoni Saray, Ramin Rojaee, Boao Song, Vitaliy Robert Yurkiv, Yayue Pan, Farzad Mashayek, and Reza Shahbazian-Yassar**

Proper distribution of thermally conductive nanomaterials in polymer batteries offers new opportunities to mitigate performance degradations associated with local hot spots and safety concerns in batteries. Herein, a direct ink writing (DIW) method is utilized to fabricate polyethylene oxide (PEO) composite polymers electrolytes (CPE) embedded with silane-treated hexagonal boron nitride (S-hBN) platelets and free of any volatile organic solvents. It is observed that the S-hBN platelets are well aligned in the printed CPE during the DIW process. The in-plane thermal conductivity of the printed CPE with the aligned S-hBN platelets is 1.031 W^{-1} K^{-1}, which is about 1.7 times that of the pristine CPE with the randomly dispersed S-hBN platelets (0.612 W^{-1} K^{-1}). Thermal imaging shows that the peak temperature (°C) of the printed electrolytes is 24.2% lower than that of the CPE without S-hBN, and 10.6% lower than that of the CPE with the randomly dispersed S-hBN, indicating a superior thermal transport property. Lithium-ion half-cells made with the printed CPE and $LiFePO_4$ cathode displayed high specific discharge capacity of 146.0 mAh g^{-1} and stable Coulombic efficiency of 91% for 100 cycles at room temperature. This work facilitates the development of printable thermally-conductive polymers for safer battery operations.

1. Introduction

In the past two decades, lithium-ion batteries have successfully penetrated the market of electric vehicles and portable electronics, mainly owing to their high-power density, long cycle life, and low self-discharge properties.[1–3] However, the safety concerns of the conventional Li-ion batteries with organic liquid electrolytes have posed significant challenges.[4,5] The formation of localized heat spots can lead to thermal runaway in batteries and safety concerns.[6–8]

Compared with carbonate-based liquid electrolytes, polymer electrolytes generally present higher electrochemical stability, better mechanical properties, and increased flexibility.[9] While polymer electrolytes are considered to be a safer option to replace the organic liquid electrolytes in Li-ion batteries, the low thermal conductivity of polymers poses challenges to the heat dissipation.[9–11] Chen et al. reported that due to the low thermal conductivity of polymer electrolytes, the thermal gradient increased in the cell stack.[12,13] As a result, the polymer electrolytes can be melted down when the battery temperature rises to the polymer melting point and causes a potential internal short circuit.[14]

Hexagonal boron nitride (hBN) materials with outstanding thermal conductivity (up to 2000 W m^{-1} K^{-1}) are considered to be promising fillers to improve the thermal conductivity of polymer separators and electrolytes.[15,16] Vishwakarma et al. presented a polyvinylidene fluoride (PVdF) gel polymer electrolytes with BN/Al_2O_3 ceramic nano/microparticles.[16] The thermal conductivity of the electrolytes could be up to 1.2 W m^{-1} K^{-1}, which was 13 times higher than the inactivated PVdF membrane. However, the internal resistance of the electrolytes also increased since the volume fraction of the electrolyte mixture was reduced by the high loading of additions. The polymer separator and electrolytes with improved thermal conductivity have been employed in Li-ion batteries to promote heat dissipation and reduce thermal stress in batteries.[17,18] Hu's group reported a thermally conductive separator coated with boron-nitride nanosheets.[17] The temperature spike of BN-coated separator was ≈32% lower than that of the pristine separator at the hotspot. The same group further fabricated PVdF-hexafluoropropylene separator with BN nanosheets via an extrusion-based printing technique.[18] Compared with the commercial separator, the maximum temperature of the printed BN-separator was lower, suggesting that the BN-separator provided a more homogenous temperature distribution.

M. Cheng, Dr. A. Ramasubramanian, M. G. Rasul, Y. Jiang, Dr. Y. Yuan, Dr. T. Foroozan, Dr. R. Deivanayagam, M. Tamadoni Saray, Dr. R. Rojaee, Dr. B. Song, Dr. V. R. Yurkiv, Prof. Y. Pan, Prof. F. Mashayek, Prof. R. Shahbazian-Yassar
Department of Mechanical and Industrial Engineering
University of Illinois at Chicago
Chicago, IL 60607, USA
E-mail: rsyassar@uic.edu

The ORCID identification number(s) for the author(s) of this article can be found under https://doi.org/10.1002/adfm.202006683.

DOI: 10.1002/adfm.202006683

Direct ink writing (DIW) provides new opportunities to fabricate polymer nanocomposites and improve battery performances. DIW is an extrusion-based printing technique which has been widely used in the field of electrochemical energy storage devices.[19–22] Compared with the conventional casting method, batteries fabricated with DIW technology are more flexible and have better compatibility with varying battery sizes and geometries.[19,20,23–25] During the printing process, the ink with appropriate rheological properties, including high viscosity, shear-thinning behavior, and the proper viscoelastic property is extruded from a fine nozzle and deposited on a substrate to form pre-programmed architecture. It is important to note that the printed materials need to have a high storage modulus to hold the desired structure.[26] Recent studies show the development of PVdF/boron nitride nanosheet composites and their introduction to textile fabrication by DIW for wearable electronics applications.[27]

In spite of the many reported studies of battery electrolyte fabrication, polyethylene oxide (PEO) electrolytes, up to our knowledge, have not been fabricated by DIW. PEO materials are the prominent choice for battery electrolytes.[5,28,29] Owing to the ethylene oxide (—EO—) units, PEO exhibits high Li-ion donor numbers and high chain flexibility which are beneficial for ion conductivity.[5] A major obstacle for DIW of PEO-based electrolytes is the low storage modulus of PEO indicating that they cannot support the weight of printed parts leading to the collapse of printed structures.

In this work, for the first time, we successfully printed PEO electrolytes free of volatile organic solvents and modified by hBN platelets. Here, we used silane-treated hBN (S-hBN) fillers where the silane coupling agent was expected to improve the compatibility between the fillers and polymer matrix due to the effect of strong hydrogen bonding interaction.[30–32] The composite ink was then used to print solid-state electrolytes via DIW. Considering that the prepared electrolytes were free of volatile organic solvents, the evaporation of solvents was not required after printing. The removal of this evaporation step is critical to prevent distortion of the printed structures. The results indicated that the addition of S-hBN platelets has several contributions: 1) provide polymer electrolytes with desired rheological properties, 2) promote the ionic conductivity of the electrolytes, 3) improve the thermal properties of the electrolytes, and 4) facilitate uniform lithium deposition for lithium metal battery. We believe that our PEO-based polymer electrolytes with embedded S-hBN is a promising printable ink material and has enormous possibilities for thermal management in energy storage applications.

2. Results and Discussion

Figure 1 illustrates the DIW process of S-hBN fillers embedded in PEO composite polymer electrolytes (CPE) without the use of any volatile organic solvents. The PEO composite electrolyte inks were prepared and stored in the syringe at 40 °C (Figure 1a). Note that the melting point (T_m) of PEO composite becomes lower than that of the pristine PEO upon the addition of Li-ion conducting ionic liquid (IL) and tetraethylene glycol dimethyl ether (TEGDME) as shown in the differential

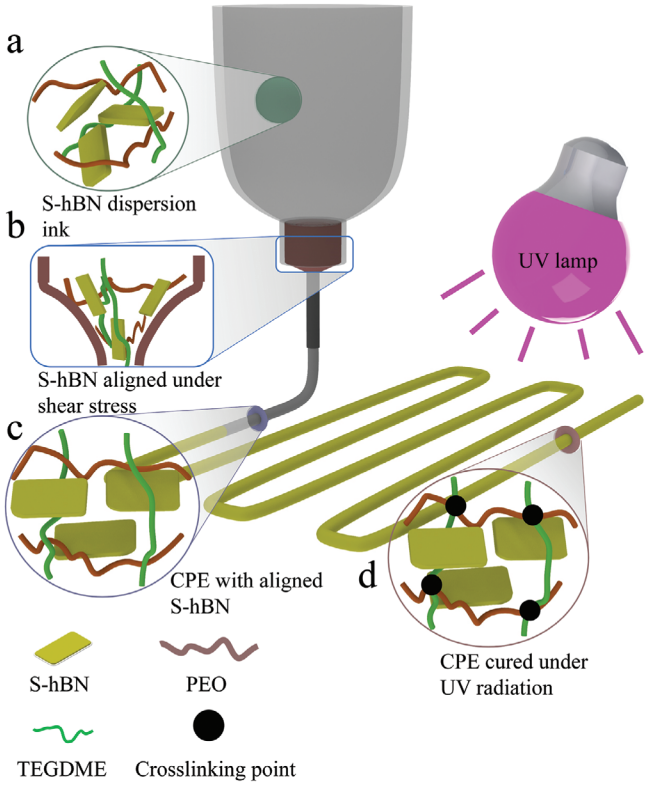

Figure 1. Schematic processing of the printing process for S-hBN modified PEO electrolytes. a) PEO-based composite electrolytes with well-dispersed S-hBN fillers are stored at 40 °C in the syringe before printing. b) S-hBN platelets are aligned by the high shear forces during ink extrusion. c) The electrolytes with aligned S-hBN fillers are printed on a substrate. d) The electrolytes are solidified under UV irradiation.

scanning calorimetry (DSC) thermograms (Figure S1, Supporting Information), which also indicates the miscibility of the composite constituents.[33] During the direct ink printing process, the randomly dispersed S-hBN fillers in composite polymer ink are likely to be aligned along the extruding direction due to the shear force induced by the extrusion nozzle (Figure 1b).[34] The electrolytes with aligned S-hBN fillers were printed on a substrate followed by a pre-programmed routine (Figure 1c). After printing, the composite electrolytes were exposed to 365 nm UV light irradiation to allow TEGDME to bind to PEO chains or interlink —EO— chains resulting in the solidification of the printed composite electrolytes (Figure 1d).

The printability of ink is significantly influenced by its rheological behaviors, especially the viscosity, fluid behavior, and viscoelastic properties.[20,35] To optimize the electrolyte ink to achieve desired rheological properties and printing behavior, the inks were prepared with varying amounts of S-hBN platelets. **Figure 2**a presents the apparent viscosity of the inks as a function of shear stress. When the shear rate increases from 10^{-2} to 1 s^{-1}, the apparent viscosity of CPE ink decreases suggesting that the polymer chains become aligned in the shear direction and the density of entanglements decreases.[36–38] Hence, the CPE ink behaves as a shear-thinning fluid. At the high shear rate of 1 s^{-1}, the apparent viscosity of CPE ink is independent of the applied shear rate indicating that all the polymer chains are

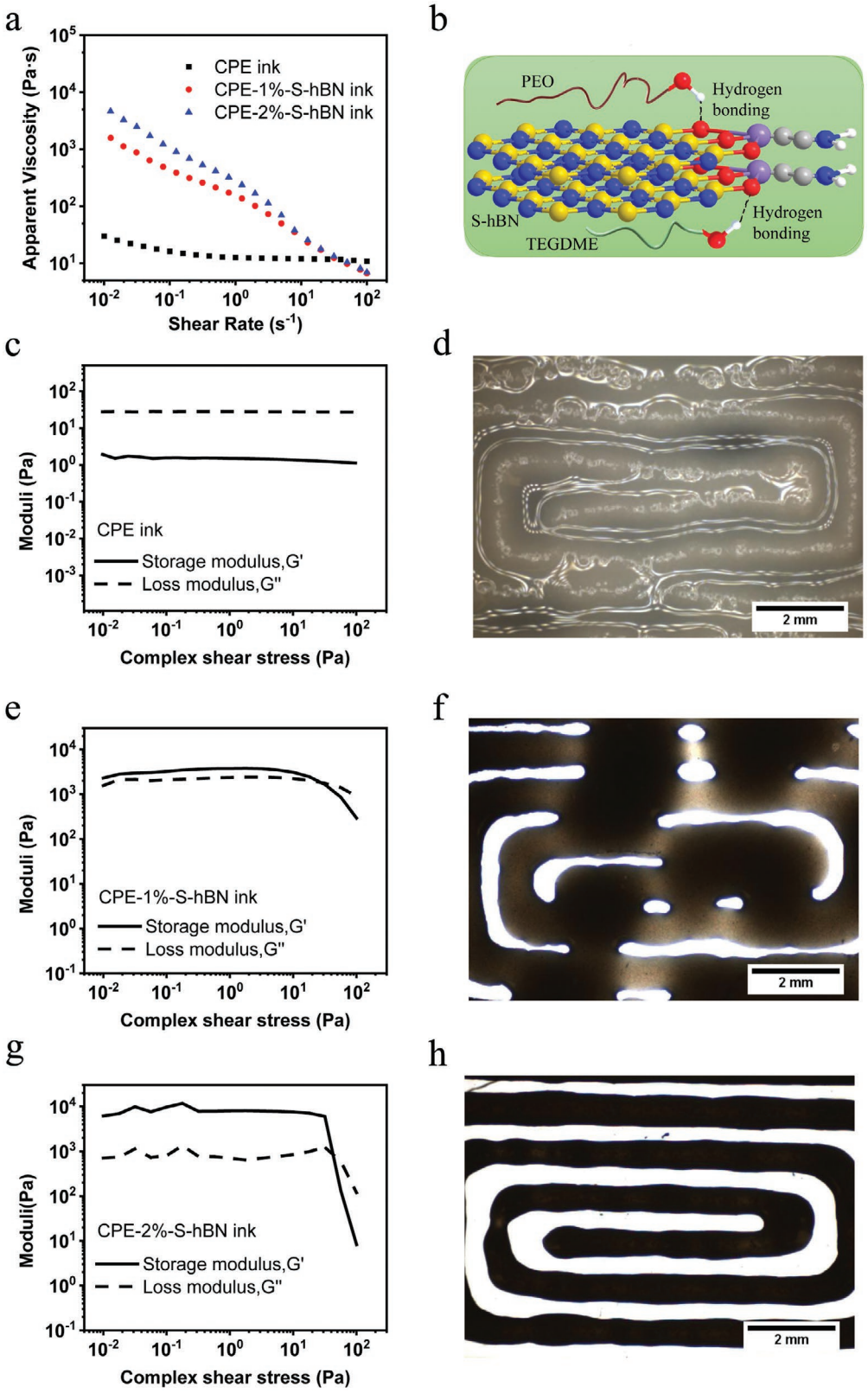

Figure 2. Rheological properties of CPE inks at 40 °C. a) Apparent viscosities as a function of shear rate of inks with and without S-hBN. b) Schematics illustration of the hydrogen bonding between the functional group of hBN and PEO/TEGDME. The storage modulus, *G′*, and loss modulus, *G″*, as a function of complex shear stress for c) CPE, e) CPE-1%-S-hBN, and g) CPE-2%-S-hBN. The optical images showing the rectangle spiral are printed with d) CPE, f) CPE-1%-S-hBN, and h) CPE-2%-S-hBN.

aligned, and the chain entanglements are eliminated.[36] Therefore, the CPE ink behaves as a Newtonian fluid. The ink modified by 1 wt% of S-hBN fillers presents two orders of magnitude higher apparent viscosity than the ink without S-hBN due to the interaction between the CPE and S-hBN. For the inks with S-hBN, both polymer and fillers are likely to be aligned in the shear direction, leading to a significant decrease of the apparent viscosity of the inks with increasing the shear rate.[37,38] Accordingly, both of the modified CPE inks behave as shear-thinning fluids, which indicate that the inks are suitable for DIW.[20] The high apparent viscosity will enhance the printability of the electrolyte inks and enable complex design patterns.[39] Increasing the filler concentration to 2 wt% leads to an increase in viscosity, which further enhances the printability of the ink.

Figure 2c shows the storage modulus (G') and loss modulus (G'') as a function of complex shear stress for the CPE ink. For the ink without S-hBN addition, the loss modulus (G'') dominates in the range of shear stress from 0.1 to 100 Pa that reveals the liquid-like response of the CPE ink. The dominance of loss modulus benefits the ink flow and extrusion through the nozzle during the printing process. However, the printed pattern completely collapses due to the low storage modulus of the ink (Figure 2d).

Compared with the CPE ink, the inks with S-hBN platelets showed different viscoelastic properties (Figure 2e,g). In the region of 10^{-1} to 10 Pa, the storage modulus (G') of the inks is higher than their loss modulus (G''), indicating that the inks exhibit a solid-like behavior. The viscoelastic property of the inks is beneficial for retaining the filament shape.[40] After the yield point, the viscous characteristic becomes the dominant behavior in the high shear stress region. The printability of the inks is endowed by the hydrogen bonds formed between the PEO/TEGDME and S-hBN platelets (Figure 2b). The PEO/TEGDME is linked with S-hBN through the non-covalent interactions, which increase storage modulus and loss modulus ≈3–4 orders of magnitude. The inks with S-hBN platelets can extrude smoothly through the nozzle at high shear stress suggesting that the weak hydrogen bonding could be easily broken down under the shear stress. Once the shear stress is released, the hydrogen bonding interactions can recover.[26] The consequence is that the recovery links enable dominance of storage modulus of the inks which leads to a solid-like behavior after printing. Although the storage modulus of the ink is higher than the loss modulus before the yield point, in such a low concentration of adding fillers (1 wt%), the gap between the moduli is relatively small which still causes some collapses of printed architecture (Figure 2f). For higher filler concentration, by contrast, the ink presents enhanced viscoelastic properties. The higher moduli of the ink enable the maintenance of the printed architecture while eliminating significant failures (Figure 2h). To further confirm the contribution of the S-hBN fillers, we investigated the rheological properties of the CPE ink with 2 wt% of pristine hBN platelets (CPE-P-hBN). As a result, the viscoelastic property of the CPE-P-hBN ink is similar to that of the CPE ink without BN additions (Figure S2, Supporting Information), indicating that the adhesion between the pristine hBN and PEO is not sufficient due to limited intermolecular interaction.[41] This insufficient interaction between the polymer matrix and pristine hBN fillers results in unfavorable rheological properties of the CPE ink.[30,31]

The S-hBN platelet fillers are aligned along longitudinal orientation of printed filaments because of the high shear force imposed on electrolyte ink during the extrusion process (**Figure 3**a). As evident in the scanning electron microscopy (SEM) images of the cross-sectional view (Figure 3b,c) and top view (Figure S3, Supporting Information), the S-hBN platelets show a high degree of alignment along the longitudinal orientation (i.e., the printing direction). Cui and co-workers reported that lithium preferred to locally grow on the hot region rather than the surrounding lower-temperature region.[42] Hence, avoiding localized high temperature is a promising strategy to reduce the risk of battery internal shorting. To study the local-temperature variation of CPEs with random distribution S-hBN (CPE-r-hBN) and CPEs with aligned S-hBN platelets (CPE-a-hBN), a point source was used to heat up the composites locally and then the temperature distribution at the surface of the composites was captured using a micro thermal imaging microscope (Figure 3d). The maximum surface temperature of the electrolyte samples reflects their heat conduction properties when the samples are exposed to the same laser heat source.[27] The electrolyte sample with a higher thermal conductivity would present a lower maximum surface temperature, suggesting that the generated heat can be efficiently dispersed from the heat spot to surrounding areas. For the electrolyte sample with a lower thermal conductivity, the localized heat cannot be dissipated effectively; as a result, the maximum surface temperature of the electrolyte sample would be higher. Figure 3e–g illustrates the temperature profiles for the CPE, CPE-r-hBN, and CPE-a-hBN, respectively. The pristine CPE shows the highest surface temperature of 389 °C (Figure S4, Supporting Information) due to its low thermal conductivity (0.457 W m^{-1} K^{-1}). On the contrary, the CPE-a-hBN exhibits the lowest surface temperature (295 °C) among the samples, which is 24.2% lower than that of the CPE, and 10.6% lower than that of the CPE-r-hBN. The results indicated that the thermal conductivity of the CPE-a-hBN composite is higher than the other two samples which could be contributed to the alignment of S-hBN fillers. The in-plane thermal conductivity of h-BN platelets has been reported to be about 550 W m^{-1} K^{-1} at room temperature, which is two orders of magnitude higher than their out-of-plane thermal conductivity (5 W m^{-1} K^{-1}).[43,44] Hence, the enhanced heat conduction behavior properties of the CPE-a-hBN could have originated from the alignment of BN fillers along the in-plane orientation, subsequently creating a heat-conduction pathway in the polymer electrolytes for heat dissipation (Figure 3h).

Through the measurement and calculation (see details in the Experimental Section), the in-plane thermal conductivity of the CPE-a-hBN is 1.031 W m^{-1} K^{-1}, which is about 1.7 times that of the CPE-r-hBN (0.612 W m^{-1} K^{-1}). The high in-plane thermal conductivity is beneficial for dissipating localized heat quickly to the surrounding area, avoiding the formation of hot spots in an operating lithium-ion battery. To quantify the effect of this difference in the in-plane and out-of-plane thermal conductivities of CPE-a-hBN and CPR-r-hBN, a finite element model in COMSOL Multiphysics was implemented, as shown in **Figure 4**a. Since the S-hBN platelet fillers are aligned along the longitudinal orientation of printed filaments, the z-direction (printing direction) is fixed and the other two directional orientations of S-hBN are uncontrolled. It is also extremely

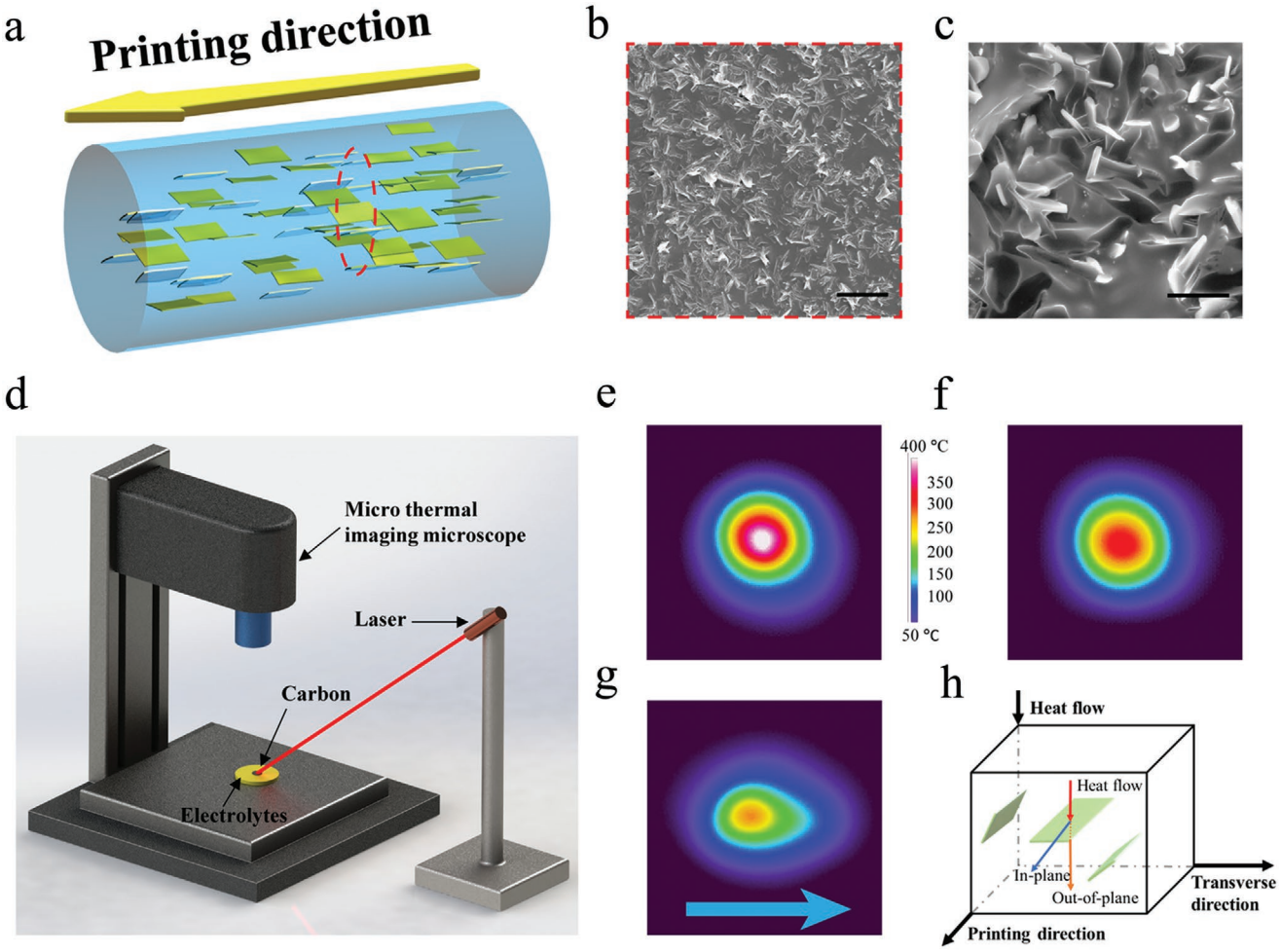

Figure 3. a) Schematic illustration of the alignment of the S-hBN platelets in the CPE host along the printing direction. b) Low magnification and c) high magnification of cross-sectional SEM image of the printed CPE-a-hBN electrolytes. Scale bar, (b) 10 µm, (c) 5 µm. d) Schematic illustration of the temperature distribution measurement setup. IR images of the temperature distribution of e) CPE, f) CPE-r-hBN, and g) CPE-a-hBN (the arrow indicates the printing direction) at laser source power of 100 µW. (h) Schematic illustration of the heat dissipation of the CPE-a-hBN heated by a laser power source (heat flow direction, red arrow). The in-plane direction (blue arrow) of the aligned S-hBN platelets is parallel to the printing direction, and the out-of-plane direction (orange arrow) of which is perpendicular to the printing direction.

challenging to identify the exact proportion of the platelet's orientation in the other two directions experimentally. However, this orientation in the other two directions can also affect the peak temperatures on the sample since lithium dendrite growth is dictated by the peak temperature.[42] The simulations, as explained in the Experimental Section, provide a good basis to understand the effect of the proportionality in alignment in the other two directions with the peak temperature when fitted to the experimental measurements. The simulations show the trend of reducing peak temperatures due to the alignment of S-hBN in the polymers (Figure 4b). The results indicate that the higher thermal conductivity of the CPE-a-hBN composite is the reason for lower peak temperatures than the other two samples.

Figure 5a compares the ionic conductivity of the PEO electrolyte composites. As a typical salt-in-polymer electrolyte, the ionic conductivity of the CPE without the IL is 0.49×10^{-4} S cm^{-1} at room temperature. The ionic conductivity of the CPE is poor due to the poor local segmental motion of the crystalline structure of PEO.[5] Moreover, based on the fractional Walden rule, the ionic conductivity of the polymers is inverse to their viscosity.[45–47] Therefore, the increase in viscosity of CPE has been reported as a reason to lead to sluggish lithium-ion transport through the electrolytes and lower the ionic conductivity.[48] Interestingly, the apparent viscosity of the CPE in the shear rate range of 10^{-2} to 10 s^{-1} was increased by adding S-hBN, while the ionic conductivity slightly increased from 0.39×10^{-3} to 0.47×10^{-3} S cm^{-1}. The enhanced ionic conductivity could be explained by the Lewis acid–base interactions between ionic species and the surface of the fillers or the increase of the amorphous portion of the polymer. A strong affinity of anions to local positive domains of the fillers promotes salt dissociation and increases the concentration of free lithium ions.[49–53]

To evaluate the electrochemical performance of the printed CPE-2%-S-hBN electrolytes, coin cells were assembled. The Li-ion cells were fabricated in the half-cell configuration with lithium iron phosphate ($LiFePO_4$ or LFP) as the cathode. The cells using the CPE without IL and CPE with IL were assembled in the same configuration for comparison. As Figure 5b shows,

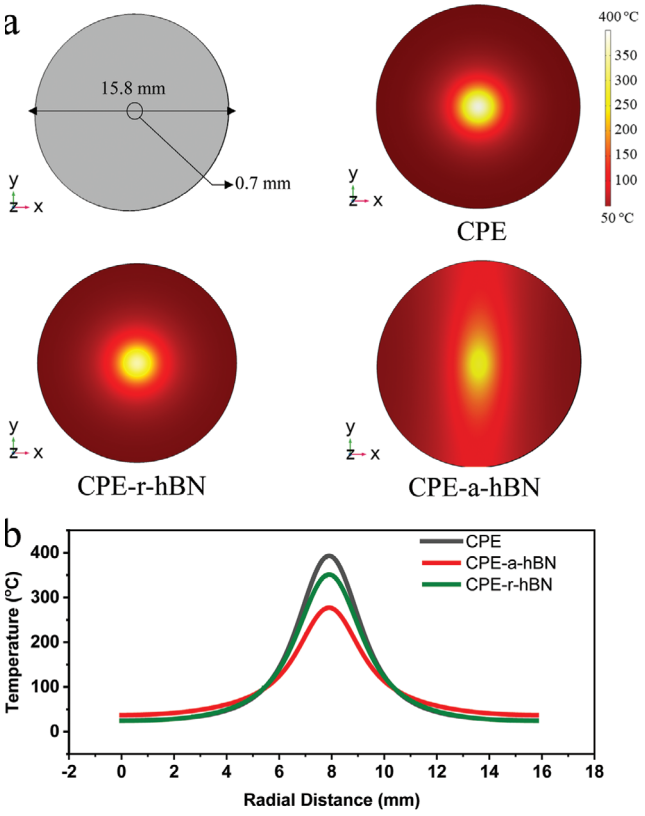

Figure 4. a) Schematic illustration of the computational domain CPE host along the printing direction. Temperature distribution of laser irradiation simulation on CPE, CPE-r-hBN, and CPE-a-hBN at laser power of 100 mW. b) The radial distribution of temperature measured along *x*-direction capturing the minimum and maximum temperatures along the surface of the CPE, CPE-r-hBN, and CPE-a-hBN.

the LFP/Li half-cell using the CPE without the IL delivers a charge and discharge capacity of 91.7 and 84.2 mAh g^{-1}, respectively. The low capacity is due to its low ionic conductivity (0.49×10^{-4} S cm^{-1}) at room temperature. The charge and discharge capacity of the LFP/Li half-cell when IL is added to CPE are 111.1 and 105.5 mAh g^{-1}, respectively. The increased capacity can be attributed to the IL, which would improve the amorphous portion of the polymer.[54,55] The charge and discharge capacity of the LFP/Li half-cell are further increased to 147.5 and 146.0 mAh g^{-1} by employing the printed CPE-2%-S-hBN as the electrolytes. Note that the Coulombic efficiency of the cell with the printed CPE-2%-S-hBN is 99.0%, which is higher than that of the cell using the CPE without IL (91.8%) and CPE with IL (95.0%). The capacity and Coulombic efficiency are improved owing to the presence of S-hBN platelets suggesting the increase in the concentration of free lithium ions.[56] Figure 5c shows the cycling performances of the cell with the printed CPE-2%-S-hBN at a current density of 17 mA g^{-1} for 100 cycles. The charge and discharge capacities of the cell are 129.4 and 118.5 mAh g^{-1} for 100 cycles at room temperature, and the Coulombic efficiency is nearly 91%.

Figure 5d shows the cycle stability for the LFP/Li half-cell using the CPE without IL, CPE with IL, and printed CPE-2%-S-hBN was cycled at a current density of 170 mA g^{-1} at 50 °C. The discharge capacity of the cell using the CPE without IL and CPE with IL fade to 2 and 60.5 mAh g^{-1} after 20 cycles. In contrast, the cell with the printed CPE-2%-S-hBN exhibits high capacity retention (93.7%) and the discharge capacity remains at 95.2 mAh g^{-1} after 20 cycles, owing to the high Li-ion conduction of the presence of S-hBN. Note that the abnormal fading of the cell using the CPE without IL might be caused by the growth of Li dendrites, which could penetrate the PEO electrolyte and cause the failure of the cell.[57]

To investigate the Li dendrite formation of the cells, the Li electrodes were disassembled from the cells after the cycling tests and were imaged by SEM. As Figure 5e shows, the Li electrodes from the cells using the CPE without IL displays the formation of dendrites with the needle-like morphology that can easily penetrate the polymer electrolyte.[58] In comparison, the Li electrodes employed in the cell using the CPE with IL (Figure S5, Supporting Information) and printed CPE-2%-S-hBN (Figure 5f) exhibit the mossy-like lithium deposition that is less likely to penetrate through the polymer electrolytes.[58,59] However, the mossy lithium deposition of the cell using the CPE with IL was non-uniform, resulting in the blockage of charge-transfer pathways and capacity decay.[60,61] Owing to the presence of the hexagonal BN platelets with enhanced thermal transport property and high stiffness, the half-cell with the printed CPE-2%-S-hBN results in a more uniform lithium deposition and thus better cycling performance at elevated temperatures and higher current densities.

Overall, the contribution of the S-hBN fillers in the CPE in Li-ion batteries are summarized as follows. The functionalization of hBN with silane enhanced the properties of PEO polymers for printing. By aligning the distribution of S-hBN platelets in PEO during DIW, the heat distribution was more effective in CPE resulting in lower surface temperature in the aligned BN composites. Owing to the improved thermal transport properties, the lithium metal battery with the aligned S-hBN in CPE exhibited a more homogenous lithium deposition and thus a better cycling performance than the Li battery cells without hBN in their CPEs. The BN additions not only contribute to enhancement in heat dissipation but also improve the ionic conductivity of the CPE. Thus, this work provides new opportunities to integrate thermally conductive materials with additive manufacturing to improve the thermal management within Li-ion batteries while minimizing the loss of battery performance.

3. Conclusion

In this work, we demonstrated the printability of PEO-polymer composite inks without the use of any volatile organic solvents, where the inks were modified by the addition of S-hBN platelets. Owing to the high apparent viscosity and proper viscoelastic properties of the polymer composite, the DIW method can be used to print polymer electrolytes for Li-ion batteries. The randomly distributed S-hBN fillers can be aligned in the direction of printing during the printing process. As a result, the electrolytes with aligned S-hBN present a high in-plane thermal conductivity of 1.031 W m^{-1} K^{-1}, which is much higher than that of PEO electrolytes with no fillers and with randomly

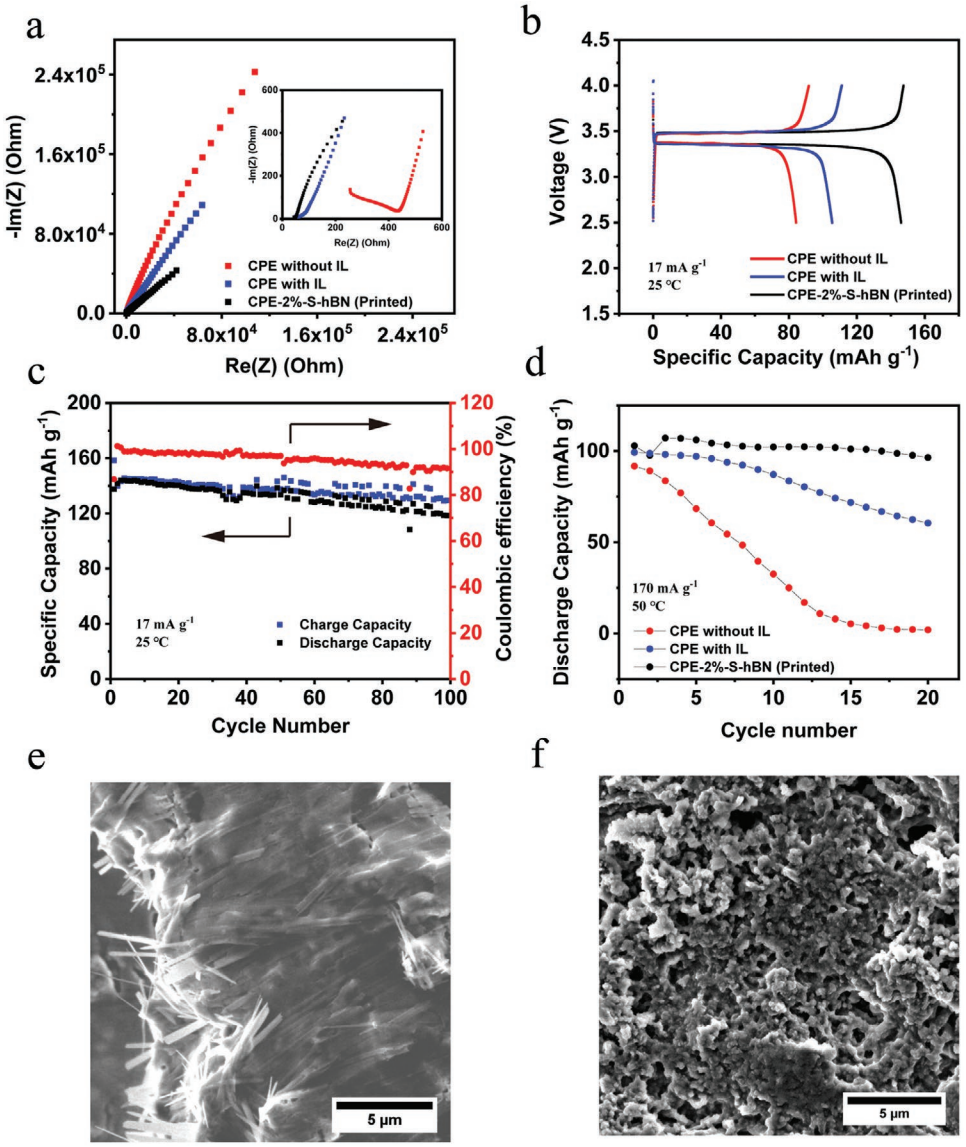

Figure 5. a) Impedance spectroscopy results for symmetric stainless cells with CPE without IL, CPE with IL, and printed CPE with 2 wt% S-hBN. The inset in (a) shows a zoom-in view at Re(Z) below 600 Ohm. b) Charge and discharge profile of LFP/Li half-cell using the CPE without IL, CPE with IL, and printed CPE-2%-S-hBN at a current density of 17 mA g^{-1} at the 2nd cycle. c) Cycling performance and Coulombic efficiency of LFP/Li half-cell with the printed CPE-2%-S-hBN at current density of 17 mA g^{-1}. d) Cycling performance of LFP/Li half-cell using the CPE without IL, CPE with IL, and printed CPE-2%-S-hBN at 170 mA g^{-1} at 50 °C. SEM image of the disassembled Li anode from the cycled half-cell using e) the CPE without IL and f) printed CPE-2%-S-hBN.

dispersed fillers. With the high in-plane thermal conductivity, the localized heat can be effectively dispersed to the surrounding region. Meanwhile, the printed composite electrolytes show a promising ionic conductivity of 0.47×10^3 S cm^{-1} at room temperature. The cell with the printed electrolytes delivers a high specific discharge capacity of 146.0 mAh g^{-1} and a stable Coulombic efficiency of 91% for 100 cycles at room temperature. Li-ion half cells assembled with the printed electrolytes exhibit stable cycling performance at high current densities and elevated temperatures due to the uniform lithium deposition resulting from the improved thermal transport properties. The S-hBN/PEO electrolyte ink is a promising electrolyte material for next-generation printable energy storage devices.

4. Experimental Section

Preparation of Inks: First, S-hBN platelets (see weight ratio in full paper) were dispersed in 2000 mg TEGDME (Sigma-Aldrich). The dispersion was sonicated for 24 h by a tip sonicator. Second, LiTFSI (EO:Li = 10:1, Sigma-Aldrich) and 1-methyl-1-propylpyrrolidinium bis(trifluoromethylsulfonyl)imide (IoLiTec Ionic Liquids Technologies) were added into the S-hBN/TEGDME dispersion and stirred for 6 h. After that, 2000 mg PEO were added into the prepared mixture and stirred for 12 h at 80 °C to form a homogenous solution. Last, 700.1 mg photoinitiator benzophenone were added into composite and mixed for 3 h at 80 °C.

Electrolyte Printing: The system used for DIW was developed by modifying a dispensing robot (Nordson EFD) to a heating-system-integrated DIW system, and the details have been reported in our previous

paper.[21] The Gauge 23 and 12.7 mm in length syringe tips (Nordson EFD) were used for electrolyte printing. The ink flow was controlled by an air-powered dispenser (Ultimus I, Nordson EFD). The nozzle pressure, printing speed, and printing temperature were 5.0 psi, 12 mm s^{-1}, and 40 °C, respectively. The printed electrolytes were cross-linked under a wavelength of 365 nm and power of 40 mW cm^{-2} UV lamp in a glovebox.

Rheological Characterization Method: The rheological properties of the inks were characterized by a Kinexus ultra+ rheometer (Malvern Instruments) with a 25 mm diameter stainless steel plate geometry. The oscillatory temperature ramp was used to get complex viscosity as a function of temperature for the electrolytes. The measurement was taken at a constant strain of 1% and angular frequency 10 rad s^{-1} at 40 °C. The shear rate sweep to get apparent viscosity as a function of shear rate (10^{-2} to 10^{2}) of the electrolytes at 40 °C. The oscillatory stress sweep was used to measure the storage modulus (G') and loss modulus (G'') as a function of shear stress (10^{-2} to 10^{2} Pa) for the inks at 40 °C and frequency of 1 Hz.

Structure and Morphology Characterization: The morphology of the samples was examined by a scanning electron microscope (Raith 100 Electron Beam Lithography System). All the samples were coated with gold in a Technics Hummer Model V sputter coater (2 min 100 $mtorr^{-1}$). The melting temperature (T_m) of each samples were measured using a Discovery DSC 2500 (TA instrument, Inc., USA). Samples (≈10 mg) were heated initially from room temperature to 150 °C at 10 °C min^{-1} heating rate and held at 200 °C for 5 min under N_2 gases. Then, samples were cooled down to –90 °C and heated up to 150 °C at 10 °C min^{-1} heating rate to find the melting temperatures.

Electrochemical Performance Test: The electrode was made of 70 wt% LFP, 15% Carbon black and 15% PVDF in NMP, and then cast onto an Al foil. The electrode was dried in a vacuum oven at 80 °C overnight. The average mass loading of LFP is 2.3 mg cm^{-2}. All cells were tested with a Bio-Logic VMP3 Potentiostat/Galvanostat electrochemical workstation and Neware battery testing system. The electrochemical impedance spectroscopy test results were collected in a frequency range of 1 MHz to 100 mHz. All the tests were carried out at room temperature.

Thermal Conductivity Measurement: The thermal conductivity of the CPE and CPE-r-hBN samples was measured by a Transient Hot Bridge (THB) measurement method thermal conductivity meter (LINSEIS). The samples were made as two circular parts with a radius of 7.5 mm and thickness of 1.5 mm. The measurement sensor (Type: G/HOTPOINT/Kaptosensor) was sandwiched by the two-sample parts and then held by the sample holder solids. The thermal conductivity of the samples was then measured by the THB—thermal conductivity analyzer.

Thermal Imaging: The thermal images were taken by a Micro Thermal Imaging Microscope System (LEADERWE). The resolution of the IR camera was 640 × 480 pixels. The IR camera with a 20 µm lens was placed right above the testing sample, where the surface temperature of the sample could be detected. A constant power of 100 mW laser was used as a point heat source to provide constant input to the electrolytes, which was placed above the polymer. The thermal mapping images of each sample were taken at the 20th second of the point heating processing.

Thermal Conductivity Calculation Using COMSOL Simulation: In this work, COMSOL Multiphysics was used to solve for the temperature distribution caused by a laser beam that is incident on the surface of a sample. Along with computational models, experiments were also performed. The heat generated inside the sample by a laser beam is transferred to the surroundings by means of convection, and radiation at the sample surface. The theoretical approach to modeling is provided in the literature.[62,63]

The temperature distribution inside the sample is found by solving Equation 1 in the computational domain shown in Figure 4a. Here, ρ is the density; C is the specific heat; k is the thermal conductivity; α is the absorption coefficient of the surface, and Q is the laser heat input.

$$\rho C \frac{\partial T}{\partial t} = \nabla \cdot (k \nabla T) + \alpha Q \tag{1}$$

In addition convective, q_c, and radiative, q_r, heat transfer boundary conditions are given by Equations (2) and (3), respectively, where h is the convective heat transfer coefficient for a natural convection with a stagnant air on top of the surface; T_∞ is the room temperature; ε is the emissivity, and σ is the Stefan–Boltzmann constant.

$$q_c = h(T_\infty - T) \tag{2}$$

$$q_r = \varepsilon\sigma\left(T_\infty^{\,4} - T^4\right) \tag{3}$$

In order to reproduce a proper description of the laser heat generation, a 2D Gaussian distribution of the intensity is used. The fundamental mode of a Gaussian beam is generally preferred, and a Gaussian heat source is provided, accordingly.[64] The usage of Gaussian beam in both x- and y-direction provides a nice circular shaped beam with peak intensity exactly at the center of the laser.

A temperature-dependent and composition-dependent material property is used to achieve a realistic description of the temperature distribution. The effective thermal conductivity of nanoparticle polymer, k, is calculated in the in-plane and the through-plane directions based on the relations in Equations (4) and (5), where x_{CPE} and x_{BN} are the volume fractions of the CPE and S-hBN, respectively, and k_{CPE} and k_{BN} are the thermal conductivities of the CPE and S-hBN in the respective in-plane and through-plane directions.

$$k_{in} = x_{CPE}\, k_{CPE} + x_{BN}\, k_{BN} \tag{4}$$

$$\frac{1}{k_{th}} = \frac{x_{CPE}}{k_{CPE}} + \frac{x_{BN}}{k_{BN}} \tag{5}$$

In order to consider the aspect ratio and anisotropy of S-hBN in the CPE-r-hBN, we used the average of k_{BN} in x- and y-directions to calculate the in-plane and through-plane values of k. The properties that are used in the model are averaged including the density and specific heat, based on the volume fraction of the interphase layer.

Since the orientation of S-hBN in the x- and y-directions are unknown, we started the simulations by assuming that the orientations are randomly distributed and there is an equal probability of having a through plane of S-hBN oriented in x-direction or y-direction. The calculation of k_{in} for the CPE-a-hBN using this theory yielded a thermal conductivity value of 1.031 W m^{-1} K^{-1} which is almost 1.7 times more than the pristine CPE surface (0.612 W m^{-1} K^{-1}). However, this value severely underpredicts the peak temperature on the surface. Based on the results from previous studies, it is reasonable to assume that the orientation of S-hBN is the only cause of the surface temperature difference between samples.[27,32,65] Therefore, we modified the averaging by adjusting the proportion of S-hBN with orientations of through plane along y-direction by increments of 5%. With 80% of S-hBN through-plane oriented along y-direction the value of the peak temperature comparable to the experimental measurements is achieved. A comparison of temperature distribution across the CPE-a-hBN is shown in Figure S6a,b, Supporting Information, for two different proportions of S-hBN orientations (50% and 80%). From these results, it could be seen that, when the peak temperatures are fitted to the experiments, a good prediction of the S-hBN orientations in x- and y-direction is achieved. Thus, these simulations provide a good understanding of the proportion of the S-hBN orientations other than the growth direction and also provide a direct evidence of drop in peak temperatures by aligning the S-hBN surface in the growth direction of the CPE.

Supporting Information

Supporting Information is available from the Wiley Online Library or from the author.

Acknowledgements

R.S.-Y., M.C., and R.D. acknowledge the financial support from NSF award CBET-1805938. The authors also acknowledge the Battery Technology Laboratory of the College of Engineering at the University of Illinois at Chicago (UIC).

Conflict of Interest

The authors declare no conflict of interest.

Keywords

boron nitride materials, composite polymer electrolytes, direct ink writing, Li-ion batteries, thermal conductivity

Received: August 8, 2020
Revised: October 1, 2020
Published online:

[1] A. S. Arico, P. Bruce, B. Scrosati, J.-M. Tarascon, W. Van Schalkwijk, *Nat. Mater.* **2005**, *4*, 366.
[2] M. Armand, J.-M. Tarascon, *Nature* **2008**, *451*, 652.
[3] A. Barré, B. Deguilhem, S. Grolleau, M. Gérard, F. Suard, D. Riu, *J. Power Sources* **2013**, *241*, 680.
[4] S. S. Zhang, *J. Power Sources* **2007**, *164*, 351.
[5] Z. Xue, D. He, X. Xie, *J. Mater. Chem. A* **2015**, *3*, 19218.
[6] Q. Wang, P. Ping, X. Zhao, G. Chu, J. Sun, C. Chen, *J. Power Sources* **2012**, *208*, 210.
[7] C.-Y. Jhu, Y.-W. Wang, C.-Y. Wen, C.-M. Shu, *Appl. Energy* **2012**, *100*, 127.
[8] W. Zhao, G. Luo, C.-Y. Wang, *J. Electrochem. Soc.* **2015**, *162*, A1352.
[9] A. M. Stephan, *Eur. Polym. J.* **2006**, *42*, 21.
[10] A. M. Stephan, K. Nahm, *Polymer* **2006**, *47*, 5952.
[11] L. Yue, J. Ma, J. Zhang, J. Zhao, S. Dong, Z. Liu, G. Cui, L. Chen, *Energy Storage Mater.* **2016**, *5*, 139.
[12] Y. Chen, J. W. Evans, *J. Electrochem. Soc.* **1996**, *143*, 2708.
[13] T. M. Bandhauer, S. Garimella, T. F. Fuller, *J. Electrochem. Soc.* **2011**, *158*, R1.
[14] H. Liu, Z. Wei, W. He, J. Zhao, *Energy Convers. Manage.* **2017**, *150*, 304.
[15] W. Luo, Y. Wang, E. Hitz, Y. Lin, B. Yang, L. Hu, *Adv. Funct. Mater.* **2017**, *27*, 1701450.
[16] V. Vishwakarma, A. Jain, *J. Power Sources* **2017**, *362*, 219.
[17] W. Luo, L. Zhou, K. Fu, Z. Yang, J. Wan, M. Manno, Y. Yao, H. Zhu, B. Yang, L. Hu, *Nano Lett.* **2015**, *15*, 6149.
[18] Y. Liu, Y. Qiao, Y. Zhang, Z. Yang, T. Gao, D. Kirsch, B. Liu, J. Song, B. Yang, L. Hu, *Energy Storage Mater.* **2018**, *12*, 197.
[19] K. Sun, T. S. Wei, B. Y. Ahn, J. Y. Seo, S. J. Dillon, J. A. Lewis, *Adv. Mater.* **2013**, *25*, 4539.
[20] K. Fu, Y. Wang, C. Yan, Y. Yao, Y. Chen, J. Dai, S. Lacey, Y. Wang, J. Wan, T. Li, Z. Wang, Y. Xu, L. Hu, *Adv. Mater.* **2016**, *28*, 2587.
[21] M. Cheng, Y. Jiang, W. Yao, Y. Yuan, R. Deivanayagam, T. Foroozan, Z. Huang, B. Song, R. Rojaee, T. Shokuhfar, Y. Pan, J. Lu, R. Shahbazian-Yassar, *Adv. Mater.* **2018**, *30*, 1800615.
[22] Y. Jiang, M. Cheng, R. Shahbazian-Yassar, Y. Pan, *Adv. Mater. Technol.* **2019**, *4*, 1900691.
[23] Y. Wang, C. Chen, H. Xie, T. Gao, Y. Yao, G. Pastel, X. Han, Y. Li, J. Zhao, K. K. Fu, L. Hu, *Adv. Funct. Mater.* **2017**, *27*, 1703140.
[24] T.-S. Wei, B. Y. Ahn, J. Grotto, J. A. Lewis, *Adv. Mater.* **2018**, *30*, 1703027.
[25] M. Cheng, R. Deivanayagam, R. Shahbazian-Yassar, *Batteries Supercaps.* **2020**, *3*, 130.
[26] E. Garcia-Tunon, S. Barg, J. Franco, R. Bell, S. Eslava, E. D'Elia, R. C. Maher, F. Guitian, E. Saiz, *Adv. Mater.* **2015**, *27*, 1688.
[27] T. Gao, Z. Yang, C. Chen, Y. Li, K. Fu, J. Dai, E. M. Hitz, H. Xie, B. Liu, J. Song, B. Yang, L. Hu, *ACS Nano* **2017**, *11*, 11513.
[28] M. Armand, *Solid State Ionics* **1983**, *9-10*, 745.
[29] K. Xu, *Chem. Rev.* **2014**, *114*, 11503.
[30] C. Harrison, S. Weaver, C. Bertelsen, E. Burgett, N. Hertel, E. Grulke, *J. Appl. Polym. Sci.* **2008**, *109*, 2529.
[31] S. Ryu, K. Kim, J. Kim, *Polym. Adv. Technol.* **2017**, *28*, 1489.
[32] J. Wang, Y. Wu, Y. Xue, D. Liu, X. Wang, X. Hu, Y. Bando, W. Lei, *J. Mater. Chem. C* **2018**, *6*, 1363.
[33] R. E. Ruther, G. Yang, F. M. Delnick, Z. Tang, M. L. Lehmann, T. Saito, Y. Meng, T. A. Zawodzinski, J. Nanda, *ACS Energy Lett.* **2018**, *3*, 1640.
[34] A. E. Jakus, E. B. Secor, A. L. Rutz, S. W. Jordan, M. C. Hersam, R. N. Shah, *ACS Nano* **2015**, *9*, 4636.
[35] J. A. Lewis, *Adv. Funct. Mater.* **2006**, *16*, 2193.
[36] E. S. Dragan, *New Trends in Nonionic (Co)Polymers and Hybrids*, Nova Science Publishers, New York **2006**.
[37] L. Raeisian, J. R. Eggers, E. M. Lange, T. Mattke, A. Bode, S. Kabelac, *Int. J. Thermophys.* **2019**, *40*, 48.
[38] H. A. Barnes, *A Handbook of Elementary Rheology*, University of Wales, Institute of Non-Newtonian Fluid Mechanics, **2000**.
[39] C. Zhu, T. Y. Han, E. B. Duoss, A. M. Golobic, J. D. Kuntz, C. M. Spadaccini, M. A. Worsley, *Nat. Commun.* **2015**, *6*, 6962.
[40] K. Fu, Y. Yao, J. Dai, L. Hu, *Adv. Mater.* **2017**, 29, 1603486.
[41] C. Zhi, Y. Bando, C. Tang, H. Kuwahara, D. Golberg, *Adv. Mater.* **2009**, *21*, 2889.
[42] Y. Zhu, J. Xie, A. Pei, B. Liu, Y. Wu, D. Lin, J. Li, H. Wang, H. Chen, J. Xu, A. Yang, C. L. Wu, H. Wang, W. Chen, Y. Cui, *Nat. Commun.* **2019**, *10*, 2067.
[43] C. Yuan, J. Li, L. Lindsay, D. Cherns, J. W. Pomeroy, S. Liu, J. H. Edgar, M. Kuball, *Commun. Phys.* **2019**, *2*, 43.
[44] C. Yuan, B. Duan, L. Li, B. Xie, M. Huang, X. Luo, *ACS Appl. Mater. Interfaces* **2015**, *7*, 13000.
[45] M. P. Longinotti, H. R. Corti, *J. Phys. Chem. B* **2009**, *113*, 5500.
[46] D. Bresser, S. Lyonnard, C. Iojoiu, L. Picard, S. Passerini, *Mol. Syst. Des. Eng.* **2019**, *4*, 779.
[47] R. Rojaee, S. Cavallo, S. Mogurampelly, B. K. Wheatle, V. Yurkiv, R. Deivanayagam, T. Foroozan, M. G. Rasul, S. Sharifi-Asl, A. H. Phakatkar, M. Cheng, S. B. Son, Y. Pan, F. Mashayek, V. Ganesan, R. Shahbazian-Yassar, *Adv. Funct. Mater.* **2020**, *30*, 1910749.
[48] N. Hasan, M. Pulst, M. H. Samiullah, J. Kressler, *J. Polym. Sci., Part B: Polym. Phys.* **2019**, *57*, 21.
[49] F. Croce, G. Appetecchi, L. Persi, B. Scrosati, *Nature* **1998**, *394*, 456.
[50] P. Jayathilaka, M. Dissanayake, I. Albinsson, B.-E. Mellander, *Electrochim. Acta* **2002**, *47*, 3257.
[51] W. Liu, N. Liu, J. Sun, P. C. Hsu, Y. Li, H. W. Lee, Y. Cui, *Nano Lett.* **2015**, *15*, 2740.
[52] S. Mogurampelly, O. Borodin, V. Ganesan, *Annu. Rev. Chem. Biomol. Eng.* **2016**, *7*, 349.
[53] R. Deivanayagam, M. Cheng, M. Wang, V. Vasudevan, T. Foroozan, N. V. Medhekar, R. Shahbazian-Yassar, *ACS Appl. Energy Mater.* **2019**, *2*, 7980.
[54] J. Choi, G. Cheruvally, Y. Kim, J. Kim, J. Manuel, P. Raghavan, J. Ahn, K. Kim, H. Ahn, D. Choi, *Solid State Ionics* **2007**, *178*, 1235.
[55] Y. Kumar, S. A. Hashmi, G. P. Pandey, *Solid State Ionics* **2011**, *201*, 73.
[56] Y. Li, L. Zhang, Z. Sun, G. Gao, S. Lu, M. Zhu, Y. Zhang, Z. Jia, C. Xiao, H. Bu, K. Xi, S. Ding, *J. Mater. Chem. A* **2020**, *8*, 9579.
[57] C. Tao, M.-H. Gao, B.-H. Yin, B. Li, Y.-P. Huang, G. Xu, J.-J. Bao, *Electrochim. Acta* **2017**, *257*, 31.
[58] P. Bai, J. Li, F. R. Brushett, M. Z. Bazant, *Energy Environ. Sci.* **2016**, *9*, 3221.
[59] Y. Lu, Z. Tu, L. A. Archer, *Nat. Mater.* **2014**, *13*, 961.
[60] Y. Zhang, F. M. Heim, N. Song, J. L. Bartlett, X. Li, *ACS Energy Lett.* **2017**, *2*, 2696.
[61] Y. Sun, Y. Zhao, J. Wang, J. Liang, C. Wang, Q. Sun, X. Lin, K. R. Adair, J. Luo, D. Wang, *Adv. Mater.* **2019**, *31*, 1806541.
[62] F. Vásquez, J. A. Ramos-Grez, M. Walczak, *Int. J. Adv. Manuf. Technol.* **2012**, *59*, 1037.
[63] A. Cocean, I. Cocean, S. Gurlui, F. Iacomi, *Sci. Bull. - Univ. "Politeh." Bucharest, Ser. A* **2017**, *79*, 263.
[64] E. Kundakcioglu, I. Lazoglu, S. Rawal, *Int. J. Adv. Manuf. Technol.* **2016**, *85*, 493.
[65] J. Chen, X. Huang, B. Sun, P. Jiang, *ACS Nano* **2018**, *13*, 337.